1 ZnO and Its Applications

K. Ellmer and A. Klein

1.1 Introduction

Zinc oxide has been investigated already in 1912. With the beginning of the semiconductor age after the invention of the transistor [1], systematic investigations of ZnO as a compound semiconductor were performed. In 1960, the good piezoelectric properties of zinc oxide were discovered [2], which led to the first electronic application of zinc oxide as a thin layer for surface acoustic wave devices [3].

Currently, research on zinc oxide as a semiconducting material sees a renaissance after intensive research periods in the 1950s and 1970s [4, 5]. The results of these earlier activities were summarized in reviews of Heiland, Mollwo and Stöckmann (1959) [6], Hirschwald (1981) [7], and Klingshirn and Haug (1981) [8]. Since about 1990 an enormous increase of the number of publications on ZnO occurred (see Fig. 1.1) and more recent reviews on ZnO have been published [9–11].

The renewed interested in ZnO as an optoelectronic material has been triggered by reports on p-type conductivity, diluted ferromagnetic properties, thin film oxide field effect transistors, and considerable progress in nanostructure fabrication. All these topics are the subject of a recently published book [11].

A major driving force of research on zinc oxide as a semiconductor material is its prospective use as a wide band gap semiconductor for light emitting devices and for transparent or high temperature electronics [12]. ZnO has an exciton binding energy of 60 meV. This is higher than the effective thermal energy at 300 K (26 meV). Therefore, excitonic gain mechanisms could be expected at room temperature for ZnO-based light emitting devices. However, a prerequisite is to prepare p-type zinc oxide, which is normally an n-type semiconductor. In the last decade, a lot of efforts were undertaken, to prepare p-type ZnO by doping with nitrogen, phosphorous, and arsenic [9, 10, 13, 14]. Maximum hole concentrations of up to $10^{19}\,\mathrm{cm}^{-3}$ and mobilities of a few $\mathrm{cm}^2\,\mathrm{V}^{-1}\,\mathrm{s}^{-1}$ at room temperature have been reported [15]. The latter are much lower than the electron mobility of $\sim 200\,\mathrm{cm}^2\,\mathrm{V}^{-1}\,\mathrm{s}^{-1}$. A severe problem is that the p-type conductivity is often not persistent, vanishing within days or weeks [13]. The fundamental thermodynamic difficulties for achieving p-type conductivity in ZnO are addressed in Sect. 1.6.1 of this chapter.

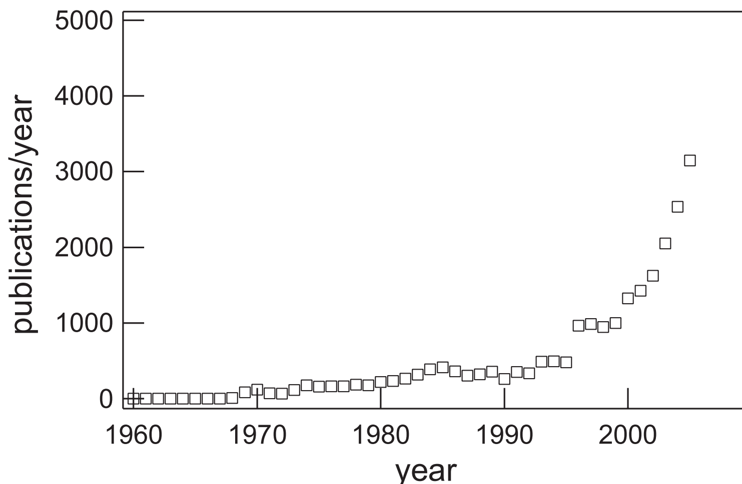

Fig. 1.1. Increase of the number of publications about *zinc oxide* (*ZnO*) over the last 40 years according to the literature data base SCOPUS

Further information on p-type doping of ZnO is given in other chapters of this book (2 and 7).

In this book the chemical, structural, optical, electrical, and interface properties of zinc oxide are summarized with special emphasis on the use of ZnO as transparent conductive electrode in thin film solar cells. This application has a number of requirements, which can be fulfilled by ZnO:

- High transparency in the visible and near infrared spectral region
- Possibility to prepare highly-doped films with free electron density $n > 10^{20}\,\mathrm{cm}^{-3}$ and low resistivity ($<10^{-3}\,\Omega\,\mathrm{cm}$)
- Good contacts to the active semiconductors (absorber layers)
- Possibility to prepare the TCO layers on large areas ($>1\,\mathrm{m}^2$) by deposition methods like magnetron sputtering or metal-organic chemical vapor deposition (MOCVD)
- Possibility to prepare ZnO films with suitable properties at low substrate temperature (<200°C for $Cu(In,Ga)(S,Se)_2$ solar cells)
- Possibility for preparation of tailored surfaces with suitable light scattering properties for light trapping, which is particularly important for Si thin film solar cells
- Low material costs, nontoxicity, and abundance in earth crust

1.2 Zinc Oxide

Zinc oxide (ZnO) is an oxidic compound naturally occurring as the rare mineral *zincite*, which crystallizes in the hexagonal wurtzite structure $P6_3mc$ [16]. The mineral zincite was discovered in 1810 by Bruce in Franklin (New Jersey,

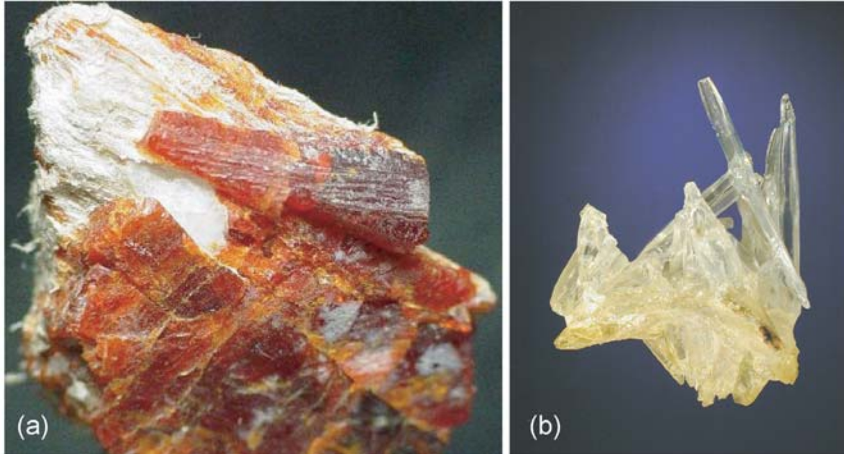

Fig. 1.2. (**a**) An orange zincite crystal from Sterling Mine, Ogdensburg, USA (collection: Rob Lavinsky, www.mineralienatlas.de/lexikon/index.php/Zinkit) and (**b**) a synthetic zinc oxide crystal (www.gc.maricopa.edu/earthsci/imagearchive/zincite755.jpg). The mineral in (a) exhibits a size of $30 \times 25 \times 6\,\mathrm{mm}^3$

USA). The zincite ore in New Jersey is an important zinc source of the USA. Other locations where zincite can be found are Sarawezza (Tuscany, Italy), Tsumeb (Namibia), Olkusz (Poland), Spain, Tasmania, and Australia.

Zincite is usually colored red or orange by manganese impurities. Photographs of zincite are shown in Fig. 1.2. Zinc oxide crystals exhibit several typical surface orientations. The most important surfaces are the (0001) and $(000\bar{1})$ (basal plane), $(10\bar{1}0)$ and $(11\bar{2}0)$ (prism planes) and $(11\bar{2}1)$ (pyramidal plane) crystal faces. In principle, the (0001) planes are terminated by Zn atoms only, while the $(000\bar{1})$ surfaces are terminated by oxygen atoms only. However, this simple picture does not hold in reality (see description of the surface structure in Sect. 4.2.1 of this book). Nevertheless, the etching behavior is noticeably different for these two surfaces [17] (see also Chap. 8).

Today, most of the zinc oxide powder produced worldwide is used in non-electronic applications for rubber production, chemicals, paints, in agriculture and for ceramics [18]. The pure powder is produced from metallic zinc, which is an abundant material in the earth's crust. Identified zinc resources of the world are about 1.9×10^9 tons [18]. The world wide mine production in 2006 was 10^7 tons [18]. In 2006, an estimated 350,000 tons of zinc was recovered from waste and scrap [18]. Of the total zinc consumed, about 55 % was used in galvanic processes for corrosion protection, 21 % in zinc-based alloys, 16 % in brass and bronze, and 8 % in other uses. Major coproducts of zinc mining and smelting, in order of decreasing tonnage, were lead, sulfuric acid, cadmium, silver, gold, and germanium.

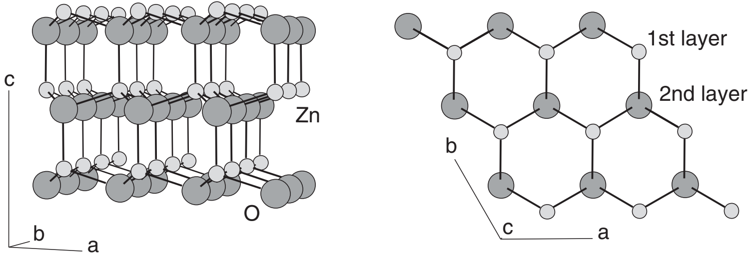

Fig. 1.3. Two views of the crystal structure of zinc oxide (ZnO). *Left*: Perspective view perpendicular to the *c*-axis. The *upper side* is the zinc terminated (0001) plane, the *bottom plane* is oxygen terminated $(000\bar{1})$. *Right*: View along the *c*-axis on the zinc terminated (0001) plane

Already in 1914, shortly after the discovery of X-ray diffraction, Bragg elucidated the crystal structure of wurtzite ZnO by X-ray diffraction, which was published in 1920 [19]. The hexagonal unit cell ($a = 0.325\,\text{nm}$, $c = 0.52066\,\text{nm}$) of ZnO, which contains 2 molecules, is shown in Fig. 1.3. The zinc atoms are surrounded by oxygen atoms in a nearly tetrahedral configuration. Along the c-axis the Zn–O distance is somewhat smaller ($d_{\text{Zn–O}}[1] = 0.190\,\text{nm}$) than for the other three neighboring oxygen atoms ($d_{\text{Zn–O}}[2] = 0.198\,\text{nm}$).

Besides the hexagonal wurtzite phase, a metastable cubic phase with the rocksalt structure is also known. Using synchrotron radiation energy-dispersive X-ray diffraction, Decremps et al. [20] measured the shrinking of the lattice cell of hexagonal ZnO up to hydrostatic pressures of 11 GPa, while Desgrenier extended his measurements even up to 56 GPa [21]. At a pressure of 9.8 GPa (at 300 K) a phase transition to the cubic phase of ZnO that exhibits the rocksalt (NaCl) structure occurs. Upon decreasing the hydrostatic pressure this phase transition is reversible in the pressure range from 2–6 GPa, depending on temperature. This means, that, in contrast to an earlier observation, the high pressure phase is not metastable at normal pressure. The temperature–pressure phase diagram of ZnO is shown in Fig. 1.4 [20]. From the XRD data at different pressures and temperatures the equation-of-state parameters for rocksalt ZnO can be calculated. The bulk modulus B at room temperature is 196 ± 5 GPa, which is higher than that of hexagonal ZnO ($B = 142.4$ GPa). The corresponding bulk moduli of Ge, Si, and GaAs are 75, 98, and 75.3 GPa [22]. This means ZnO exhibits a high covalent bonding energy.

1.3 Properties of ZnO

In Table 1.1 a number of properties of zinc oxide are summarized in comparison to other transparent conducting oxides and to silicon.

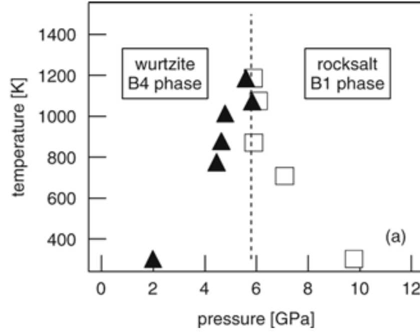

Fig. 1.4. Phase diagram of ZnO. The *squares* mark the wurtzite (B4) – rocksalt (B1), the *triangles* the B1–B4 transition [20]. The hysteresis of the transition, which extends from 9.8 to 2 GPa at 300 K, depends on the temperature and is absent for $T > 1\,300$ K

Today, the most important TCOs for electrode applications are In_2O_3, SnO_2, and ZnO, which are typically doped using tin (In_2O_3:Sn = ITO), fluorine (SnO_2:F = FTO), and Al (ZnO:Al = AZO), respectively [24, 33, 34]. The transparency is due to their optical band gaps, which is $\geq$3.3 eV, leading to a transparency for wavelength >360 nm. The direct gap of In_2O_3 is $E_{g,d} =$ 3.6–3.75 eV [35, 36]. An indirect optical gap of $E_{g,d} = 2.6$ eV has also been reported for this material [35]. However, literature is not yet conclusive on the existence of an indirect gap (see discussions in [37–39]).

CdO, the first discovered and applied transparent conductor [40], which also exhibits the highest reported conductivity (see compilation of data in [41]), is less used today because of its toxicity and its low optical band gap ($E_{g,d} = 2.2$ eV, $E_{g,i} = 0.55$ eV [42]). Photoelectron spectra indicate, however, that the band gap is ~1 eV [43]. Although the (direct) optical gap is increased for degenerate doping due to the Burstein–Moss effect [44], it remains difficult to prepare noncolored CdO films.

More recently also TCOs with multiple cations have been investigated by a number of groups [34,45,46]. The search for new TCO materials is partially related to the desired replacement of indium due to its limited availability, but also to achieve better functionality due to modified interface properties or the requirement of even higher conductivity at the same transparency level. The latter might be achieved by TCOs with higher carrier mobilities (see also Chap. 2). In addition, a number of p-type TCOs have been identified [47–53]. These typically contain metals with shallow d-levels (mainly Cu 3d). In consequence, these materials can have high carrier concentrations, but typically lack of high mobility [54, 55]. $CuInO_2$ has been shown to exhibit both n- and p-type conductivity [51,52]. The transparency of this material is, however, due to an optically forbidden transition of the fundamental gap [56].

The electrically active band gap is, therefore, considerably lower than the apparent optical gap.

Of the semiconductors in Table 1.1 only ZnO exhibits piezoelectricity, i.e., the generation of electrical charges when subjected to a mechanical deformation. This is caused by the polarity of zinc oxide, i.e., the absence of inversion symmetry in this crystal lattice. Other materials that exhibit piezoelectricity are e.g., α-quartz (SiO_2), $LiNbO_3$, ZnS, turmaline, saccharose, or liquid crystals. The high piezoelectric or electromagnetic coupling factor of ZnO, which is defined as the square root of the ratio of electrostatic energy and the mechanical deformation energy stored in the material

Table 1.1. Abundance of the metal in the earths's crust, optical band gap E_g (d: direct; i: indirect) [23, 24], crystal structure and lattice parameters a and c [23, 24], density, thermal conductivity κ, thermal expansion coefficient at room temperature α [25–27], piezoelectric stress e_{33}, e_{31}, e_{15} and strain d_{33}, d_{31}, d_{15} coefficients [28], electromechanical coupling factors k_{33}, k_{31}, k_{15} [29], static $\varepsilon(0)$ and optical $\varepsilon(\infty)$ dielectric constants [23, 30, 31] (see also Sect. 3.3, Table 3.3), melting temperature of the compound T_m and of the metal T_m(metal), temperature T_{vp} at which the metal has a vapor pressure of 10^{-3} Pa, heat of formation ΔH_f per formula unit [32] of zinc oxide in comparison to other TCOs and to silicon

Parameter	Unit	ZnO	In_2O_3	SnO_2	Si
Mineral		Zincite		Cassiterite	Silicon
Abundance	ppm	40	0.1	40	2.6×10^5
E_g	eV	3.4 (d)	3.6 (d)	3.6 (d)	1.12 (i)
Lattice		Hexagonal	Cubic	Tetragonal	Cubic
structure		Wurtzite	Bixbyite	Rutile	Diamond
Space group		$P6_3mc$	$Ia3$	$P4_2/nmm$	$Fd3m$
(number)		186	206	136	227
a, c	nm	0.325, 0.5207	1.012	0.474, 0.319	0.5431
Density	$\mathrm{g\,cm^{-3}}$	5.67	7.12	6.99	2.33
κ	$\mathrm{W\,m^{-1}\,K^{-1}}$	$69_{\parallel}$, $60_{\perp}$		$98_{\parallel}$, $55_{\perp}$	150
α	10^{-6}/K	$2.92_{\parallel}$, $4.75_{\perp}$	6.7	$3.7_{\parallel}$, $4.0_{\perp}$	2.59
e_{33}, e_{31}, e_{15}	$\mathrm{C\,m^{-2}}$	1.32, –0.57, –0.48			
d_{33}, d_{31}, d_{15}	$10^{-12}\mathrm{C\,N^{-1}}$	11.7, –5.43, –11.3			
k_{33}, k_{31}, k_{15}		0.47, 0.18, 0.2			
$\epsilon(0)$		$8.75_{\parallel}$, $7.8_{\perp}$	8.9	$9.58_{\parallel}$, $13.5_{\perp}$	
$\epsilon(\infty)$		$3.75_{\parallel}$, $3.70_{\perp}$	4.6	$4.17_{\parallel}$, $3.78_{\perp}$	
T_m	°C	1,975	1,910	1,620[a]	1,410
T_m (metal)	°C	420	157	232	1,410
T_{vp}	°C	208	670	882	
ΔH_f	eV	3.6	9.6	6.0	–

[a] Decomposes into SnO and O_2 at 1,500°C

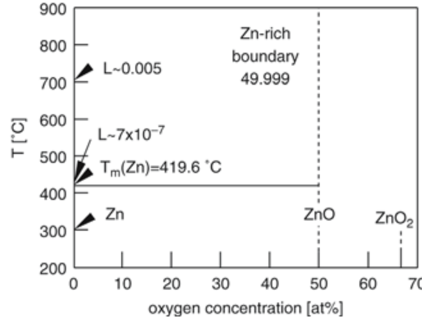

Fig. 1.5. Binary Zn–O phase diagram [58]. Above 200°C only ZnO is stable. L indicates the solubilities of oxygen in Zn at different temperatures. T_m(Zn) is the melting point of Zn (419.6°C)

($k_{ij}^2 = d_{ij}^2/e_{ij}/s_{ij}$) [57], led to one of the first electronic applications of zinc oxide in surface-acoustic wave devices (see Sect. 1.7). The piezoelectricity of ZnO also induces a charge carrier scattering process (piezoelectric mode scattering, see Chap. 2, Sect. 2.1.2), which is important for the electron mobility in ZnO single crystals at low temperatures (100 K). For highly-doped ZnO films, there are indications that the piezoelectricity influences the carrier transport even at room temperature (see Sect. 2.2.3).

The binary oxygen–zinc phase diagram is depicted in Fig. 1.5 [58]. Above 200°C only the binary compound ZnO is stable. At low temperatures also zinc peroxide (ZnO_2) is reported, which can be prepared by chemical synthesis [59]. The melting point of ZnO is 1975°C. The sublimation of ZnO occurs congruently by decomposition to the gaseous elements according to:

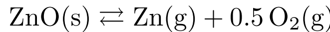

$$ZnO(s) \rightleftarrows Zn(g) + 0.5\,O_2(g)$$

All three oxides listed in Table 1.1 exhibit high melting points of 1,600–2,000°C. However, it has to be kept in mind that these oxides decompose into the elements below their melting points if the oxygen partial pressure is too low. This is important for the deposition of such oxides at higher substrate temperatures (see Chaps. 5–7). The melting points of the metals in ZnO, In_2O_3, and SnO_2 are quite low. Zinc also has a high vapor pressure at typical substrate temperatures during deposition (<600 K). In contrast indium and tin have lower vapor pressure, and reevaporation of metal during growth at elevated substrate temperature is less important. The formation energies of the oxides, related to one metal atom, are 3.6 eV (ZnO), 4.8 eV (In_2O_3), and 6 eV (SnO_2) explaining the increased thermodynamic stability of these oxides going from ZnO to SnO_2.

The vapor pressure of ZnO is high already at about 1,400°C [60], which makes it difficult to grow single crystals from its own melt. The stoichiometric width of ZnO below 600°C is rather narrow. For temperatures higher than

600°C Hagemark and Toren [61] measured the Zn–$Zn_{1+x}O$ phase boundary by an electro-chemical method and by Hall and conductivity measurements assuming that excess zinc constitutes a shallow donor in ZnO. New measurements of Tomlins et al. [62] suggest that Hagemark and Toren actually measured the phase boundary Zn–ZnO_{1-x}, i.e., the concentration of oxygen vacancies. Recently, Lott et al. [63] measured the excess zinc in the vapor phase directly by optical absorption. Their results are shown in Fig. 1.6.

The temperature dependence of the lattice parameters a and c of ZnO were measured by Khan [25] and Reeber [26] and are displayed in Fig. 1.7. For low temperatures ($T < 200$ K) ZnO exhibits a very small thermal expansion. For temperatures higher than 300 K, the thermal expansion of the a and c axis are linearly dependent on T, which means that the thermal expansion

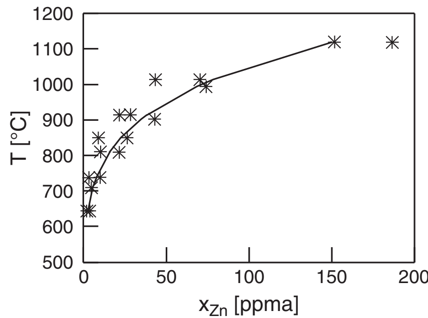

Fig. 1.6. Zinc excess x_{Zn} according to Lott et al. [63] near the stoichiometric composition $Zn_{1+x}O$ in the temperature range 600–1,100° C

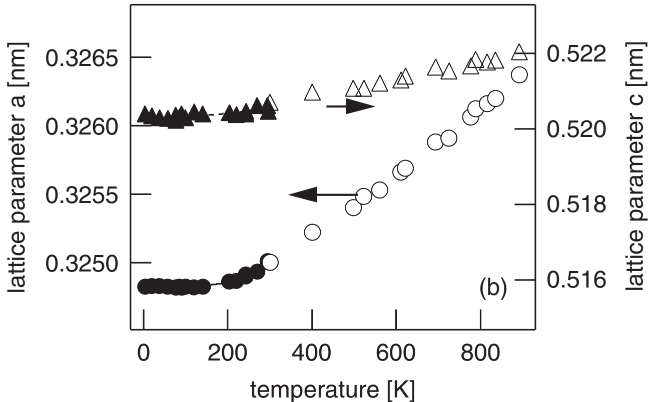

Fig. 1.7. Thermal expansion of ZnO (wurtzite) along the a and the c-axis in the temperature ranges from 4 to 296 K [26] (*full symbols*) and from 300 to 892 K [25] (*open symbols*), which fit very well to each other

coefficients $\alpha_{\|/\perp} = (\mathrm{d}a, \mathrm{d}c)/\mathrm{d}T$ are constant. The linear thermal expansion coefficient at room temperature is $\alpha_{\|} = 2.9 \times 10^{-6}\,\mathrm{K}^{-1}$ and $\alpha_{\perp} = 4.75 \times 10^{-6}\,\mathrm{K}^{-1}$, which is lower than that of In_2O_3 and SnO_2 and only slightly higher than that of silicon (see Table 1.1).

1.4 Material Preparation

1.4.1 Growth of ZnO Single Crystals

Zinc oxide single crystals were grown already in 1935 by Fritsch by evaporation and condensation of ZnO from pressed and sintered cylinders in air at about 1,450°C [64]. Later especially three methods were used for crystal growth:

- Hydrothermal growth in autoclaves at temperatures up to 450°C and pressures up to 2,500 bar [65, 66]
- Growth from the gas phase by oxidation of Zn vapor at temperatures between 1,100 and 1,400°C [57, 67]
- Growth from melts of salts with low melting temperature ($ZnBr_2$) [68].

Today, only the first two methods are used for the growth of single crystals [69]. However, recently also the growth of ZnO from its pressurized melt in a cold crucible was demonstrated [70]. This technique, which uses oxygen pressures up to 100 bar, is scalable to crystal diameters larger than 125 mm. A new, promising method, avoiding the temperature-gradient problems with a cold crucible, uses a hot iridium crucible [71]. To prevent the oxidation (burning) of the iridium crucible the growth is performed in a self-adjusting gas atmosphere of CO_2.

Single crystalline ZnO wafers are commercially available from different companies as listed in Table 1.2. Photographs of a ZnO single crystal and of wafers are shown in Fig. 1.8.

1.4.2 Deposition of ZnO Thin Films

ZnO thin films can be prepared by a variety of techniques such as magnetron sputtering, chemical vapor deposition, pulsed-laser deposition, molecular beam epitaxy, spray-pyrolysis, and (electro-)chemical deposition [24, 74]. In this book, sputtering (Chap. 5), chemical vapor deposition (Chap. 6), and pulsed-laser deposition (Chap. 7) are described in detail, since these methods lead to the best ZnO films concerning high conductivity and transparency. The first two methods allow also large area depositions making them the industrially most advanced deposition techniques for ZnO. ZnO films easily crystallize, which is different for instance compared with ITO films that can

Table 1.2. Parameters of commercially available zinc oxide single crystals

Parameter	Unit	ZNT	CI	ML	TDC
Method		s-CVT	PM	HT	HT
T	°C	1,100	2,000	330	300–400
P	MPa			50	<100
d	mm	51	130	51	51
ρ	Ω cm	0.3	0.35	500–1 000	390
$N_D - N_A$	cm^{-3}	1×10^{17}	9×10^{16}		8×10^{13}
μ	$cm^2 V^{-1} s^{-1}$	209	200		200
$N_{disl.}$	cm^{-2}			<50	<300
Ref.		[72]	[70]	[73]	[66]

Abbreviations and symbols denote ZNT: ZN Technology Inc. (formerly Eagle Pitcher), Brea, USA; CI: Cermet Inc., Atlanta, USA; ML: Mineral Ltd., Alexandrov, Russia; TDC: Tokyo Denpa Co., Tokyo, Japan; s-CVT: seeded chemical vapor transport; PM: pressurized melt; HT: hydrothermal; T: growth temperature; P: growth pressure; d: dimension; ρ: resistivity; $N_{D,A}$: donor or acceptor concentration; μ: Hall mobility; N_{dis}: dislocation density

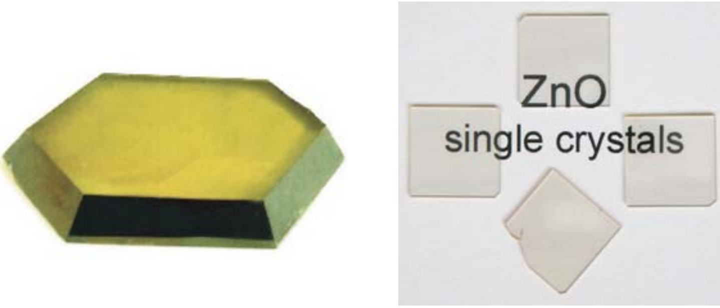

Fig. 1.8. (**a**) Photographs of a hydrothermally grown zinc oxide single crystal (Mineral Ltd., Alexandrov, Russia) and (**b**) of zinc oxide wafers prepared from such crystals (Crystec GmbH, Berlin, Germany). The as grown crystal in (a) has a maximum size of 70 mm [73]. The size of the crystals in (b) is $10 \times 10 \times 0.5\,mm^3$

be grown as amorphous films [75]. ZnO films exhibit mostly a (0001) texture, i.e., the c-axes of the crystallites are perpendicular to the substrate surface [24, 74]. Plasma-assisted processes (magnetron sputtering, pulsed-laser ablation) induce a pronounced c-axis (0001) texture. While on amorphous substrates or silicon ZnO forms polycrystalline films without an in plane alignment, epitaxial films, i.e., films with an in and out of plane alignment can be grown on oxide single crystalline substrates (sapphire-Al_2O_3, $LiNbO_3$, MgO etc.) even at room temperature [76]. Structural and electrical properties of polycrystalline and epitaxial films are compared in Sect. 2.2.3.

1.4.3 Preparation of ZnO Nanostructures

The first experiments on single crystal growth of ZnO [64, 77] showed that under equilibrium conditions ZnO grows preferentially along the (0001) axis, leading to needle-like crystals with dimensions in *c* direction of some millimeter. The first reported electrical and optical measurements on ZnO single crystals were performed on such pencil-like crystals with a hexagonal cross section [2] (see Chap. 2). Later, under nonequilibrium conditions a large variety of ZnO nanostructures were synthesized. Yamada and Tobisawa obtained ZnO plates, columns, pyramids, stellar-shaped crystals, spheres, whiskers, and dendrites under the extreme nonequilibrium conditions of a converging shock-wave using an explosive charge [78]. In the last 10 years other techniques were used to grow ZnO nanostructures: pulsed-laser ablation (see also Chap. 7), magnetron sputtering [79], chemical-vapor deposition [80], and chemical solution preparation [81]. ZnO nanostructures exhibit a high crystalline quality as inferred from cathode- and photoluminescence measurements [82]. A review on ZnO nanorods was given recently by Yi et al. [83]. Information on ZnO nanostructures can also be found in [9, 11].

Figure 1.9 shows scanning electron micrographs of an array of ZnO nanowires grown on a magnetron-sputtered ZnO film on a fluorine-doped SnO_2 covered glass substrate. Because of the strongly *c*-axis oriented growth of the magnetron-sputtered ZnO film, the ZnO nanowires are very well-aligned vertically. The hexagonal cross section is clearly visible. Depending on the preparation conditions, diameter and length of the nanowires can be adjusted [79].

Possible applications of ZnO nanostructures are UV lasers (up to now only with optical excitation) [84], chemical sensors [85], or transparent substrates for thin film solar cells, e.g. as an alternative to TiO_2 in injection type solar cells or in organic solar cells [79, 86, 87]. In the latter two applications the increased effective surface of arrays of ZnO nanowires leads to

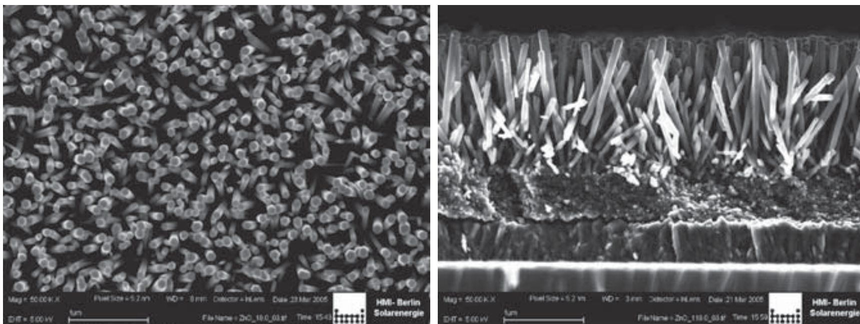

Fig. 1.9. Plain view (*left*) and cross-sectional view (*right*) of ZnO nanowires prepared from a chemical solution on a magnetron-sputtered ZnO film on fluorine-doped SnO_2 on glass, which are used as a substrate for dye-sensitized solar cells [79]

increased sensitivity or absorption. Recently, a new, interesting application of ZnO nanowires was reported [88]. Combining ZnO nanowires with zig–zag structured electrodes, a device that is able to convert ultrasonic energy into a voltage was demonstrated. In this arrangement the piezoelectric effect of ZnO (see Table 1.1) is used to extract a voltage due to mechanical bending of the nanowires.

1.5 Electronic Structure of ZnO

ZnO is a tetrahedrally bonded semiconductor. The electronic structure of tetrahedrally bonded materials with diamond, zincblence, wurtzite, or chalcopyrite structure is very similar [23, 89, 90]. Except for symmetry, the electronic structures of zincblende and wurtzite modifications are mostly identical. The cation and anion s- and p-orbitals form sp^3-hybrids, which overlap forming bonding and antibonding combinations. The electronic states at the valence band maximum are mainly derived from anion p-states and are, therefore, threefold degenerate. However, the degeneracy is lifted by spin-orbit splitting and also by noncentrosymmetric crystal fields. The latter is pronounced e.g., in the chalcopyrite structure with a I–III–VI_2 (e.g., $CuInSe_2$) or a II–IV–V_2 (e.g., $ZnSnP_2$) composition [91] but also occurs in ZnO [23]. At liquid He temperatures the three valence bands are at 0, 4.9, and 48.6 meV binding energy with respect to the valence band maximum, respectively [92]. In the I–III–VI_2 chalcopyrites, there is further a considerable hybridization between the anion p-states and the low lying d-states of the group I cation, which leads to a lowering of the optical gap compared with the binary II–VI analogues [93, 94]. In literature this band gap anomaly is often indicated as *p–d repulsion* as the presence of the metal (Cu, Ag) d-states leads to an upward shift of the valence band maximum [93–95].

In LCAO[1] theory the valence band maximum of a tetrahedrally bonded semiconductor is derived from the anion p-levels and its energy given by [89]:

$$E_{\mathrm{VB}} = \left(E_{\mathrm{p}}^{\mathrm{a}} + E_{\mathrm{p}}^{\mathrm{c}}\right)/2 - \left\{\left[\left(E_{\mathrm{p}}^{\mathrm{a}} + E_{\mathrm{p}}^{\mathrm{c}}\right)/2\right]^2 + \left[1.28\hbar^2/\left(m_{\mathrm{e}}d^2\right)\right]^2\right\}^{1/2}, \quad (1.1)$$

where $E_{\mathrm{p}}^{\mathrm{a}}$ and $E_{\mathrm{p}}^{\mathrm{c}}$ are the p orbital energies of the anion and the cation, m_{e} is the free electron mass and d the interatomic spacing, respectively. According to (1.1), a lower valence band maximum has to be expected for anions with a larger binding energy of the p levels. The binding energy[2] of the p orbitals increases monotonically from Te (9.54 eV) over Se (10.68 eV) and S (11.6 eV) to O (16.72 eV) [89]. In fact the valence band offsets between II–VI semiconductors, which are displayed in Fig. 1.10, nicely follow the trend calculated by Wei and Zunger using density functional theory [95]. They correspond well with experimental determinations (see Chap. 4).

[1] Linear combination of atomic orbitals [89].

[2] Hartree–Fock atomic term values are used in LCAO theory [89].

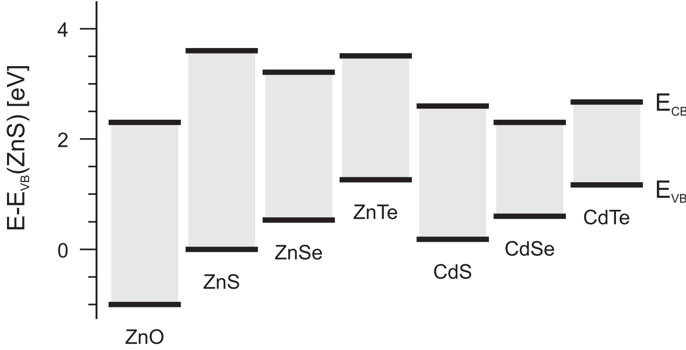

Fig. 1.10. Band alignment between II–VI compounds according to density functional theory calculations by Wei and Zunger [95]. The energy of the valence band maximum of ZnS is arbitrarily set to 0 eV. A comparison to experimental results is presented in Fig. 4.18 in Sect. 4.3.1 (page 150)

To understand the full details of the band alignment, the contribution of the cation d-states also needs to be considered [95]. Because of the low lying O 2p levels, the interaction between the Zn 3d and the anion p states in ZnX (X = O, S, Se, Te) compounds is strongest for ZnO [43, 96–98]. This also explains the anomaly of the band gaps for the ZnX compounds (see Fig. 1.10): While the band gap generally increases with lower anion mass, the gap of ZnO (3.4 eV) is smaller than the gap of ZnS (3.7 eV). However, instead of shifting the valence band maximum upward in energy, as in the case of the chalcopyrites [93, 94] and other II–VI compounds [94, 95], the band alignments given in Fig. 1.10 rather suggest a lowering of the ZnO conduction band minimum as the valence band maximum of ZnO roughly follows the trend with decreasing anion mass.

As the mixing between the anion p and the cation d levels affects the energetic positions of the energy bands, it is particularly important for the function of quantum well structures. The band alignment between the barrier and the well material is important for establishing the energy levels and, therefore, the optical transitions. ZnO-based quantum well structures can be prepared by alloying of ZnO with MgO or CdO [99–104]. $Zn_{1-x}Mg_xO$ retains the wurtzite structure for Mg admixtures up to $x \approx 0.5$ [99, 102–104] resulting in a variation of the optical gap with x from 3.4–4.5 eV [104]. More details on the optical properties of ZnO and (Zn,Mg)O are presented in Chap. 3. As there are no d levels in Mg, alloying of ZnO with MgO therefore affects the energy positions of the band edges according to the different s and p atomic levels (1.1) and by modifying the interaction between the anion p and the cation d states.

Figure 1.11 shows an experimental determination of the band alignment at the ZnO/(Zn,Mg)O interface using optical spectroscopy of quantum well structures [100]. The data indicate that the larger band gap of (Zn,Mg)O is

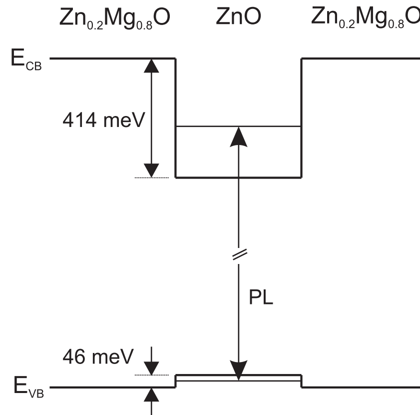

Fig. 1.11. Energy-level alignment between ZnO and (Zn,Mg)O as determined by optical spectroscopy [100]. The energy-level alignment agrees with a recent indirect determination using photoelectron spectroscopy [105]. The difference of the band gaps is almost fully accomplished by a conduction band offset

almost completely accomplished by an upward shift of the conduction band energy. This result is in good agreement with a recent indirect determination of the band alignment using photoelectron spectroscopy [105] (for more information on band alignments see Chap. 4).

1.6 Intrinsic Defects in ZnO

1.6.1 Thermodynamic Properties

Intrinsic point defects are deviations from the ideal structure caused by displacement or removal of lattice atoms [106,107]. Possible intrinsic defects are vacancies, interstitials, and antisites. In ZnO these are denoted as V_{Zn} and V_O, Zn_i and O_i, and as Zn_O and O_{Zn}, respectively. There are also combinations of defects like neutral Schottky (cation and anion vacancy) and Frenkel (cation vacancy and cation interstitial) pairs, which are abundant in ionic compounds like alkali-metal halides [106,107]. As a rule of thumb, the energy to create a defect depends on the difference in charge between the defect and the lattice site occupied by the defect, e.g., in ZnO a vacancy or an interstitial can carry a charge of ± 2 while an antisite can have a charge of ± 4. This makes vacancies and interstitials more likely in polar compounds and antisite defects less important [108–110]. On the contrary, antisite defects are more important in more covalently bonded compounds like the III–V semiconductors (see e.g., [111] and references therein).

The formation of one mole of a defect requires an energy ΔH_d. The distribution of the created defects on the available sites N increases the entropy

S of the system. The change in free energy of a crystal by defect formation $\Delta G_{\mathrm{d}} = \Delta H_{\mathrm{d}} - TS$ has a minimum at a defect concentration

$$N_{\mathrm{d}} = N \exp(-\Delta H_{\mathrm{d}}/k_{\mathrm{B}\mathrm{T}}), \tag{1.2}$$

which defines the number of defects in thermodynamic equilibrium.

An important aspect of intrinsic defects is the dependence of their formation energy on the chemical potential and the Fermi level position in the gap [112]. The chemical potential corresponds to the concentration of a species, which is for gases related to its partial pressure. An increasing partial pressure of oxygen, e.g., leads to a lowering of ΔH_d for defect reactions that add oxygen or remove Zn (O_i, V_{Zn}) and vice versa. For charged defects, the defect formation enthalpy directly depends on the Fermi energy, which is the chemical potential of the electrons (and holes).[3] This dependency is schematically sketched in Fig. 1.12.

A donor type defect e.g., can be neutral or positively charged depending on its occupation, which is given by the Fermi level position with respect to the defect energy E_D. Donors are occupied (neutral) when the Fermi level is above the defect level and unoccupied (charged) when the Fermi level is below the defect level. The electron from the donor is transferred to its reservoir whose energy is represented by the Fermi energy. This leads to an energy gain $\delta = q(E_{\mathrm{D}} - E_{\mathrm{F}})$, where q is the charge of the donor. The energy gained by lowering the Fermi level toward the valence band maximum generally decreases the formation enthalpy of the donors. As intrinsic defects in ZnO carry a charge of 2, the maximum energy gain from a variation of the Fermi

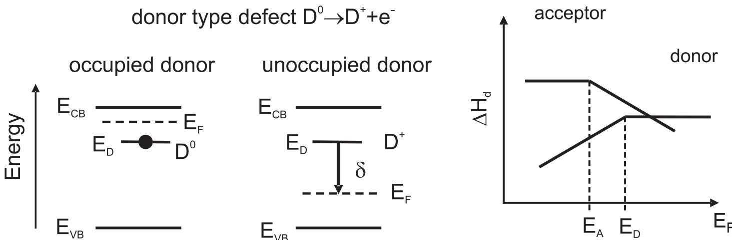

Fig. 1.12. Dependence of the defect formation enthalpy ΔH_{d} on the Fermi energy. An occupied donor ($E_{\mathrm{F}} > E_{\mathrm{D}}$) is electrically neutral and ΔH_{d} does not depend on E_{F}. The unoccupied donor ($E_{\mathrm{F}} < E_{\mathrm{D}}$) is positively charged and the electron(s) released from the donor is(are) transferred to the electron reservoir (E_{F}) leading to an energy gain δ. The defect formation enthalpy hence decreases with decreasing Fermi energy. The resulting variation of defect formation enthalpy with Fermi energy for donor and acceptor defects is shown on the *right*. The crossing of the neutral and the charged defect state identifies the energy position of the defect states (E_{D} and E_{A})

[3] The treatment is for homogeneous materials (bulk) where the electrostatic potential is constant.

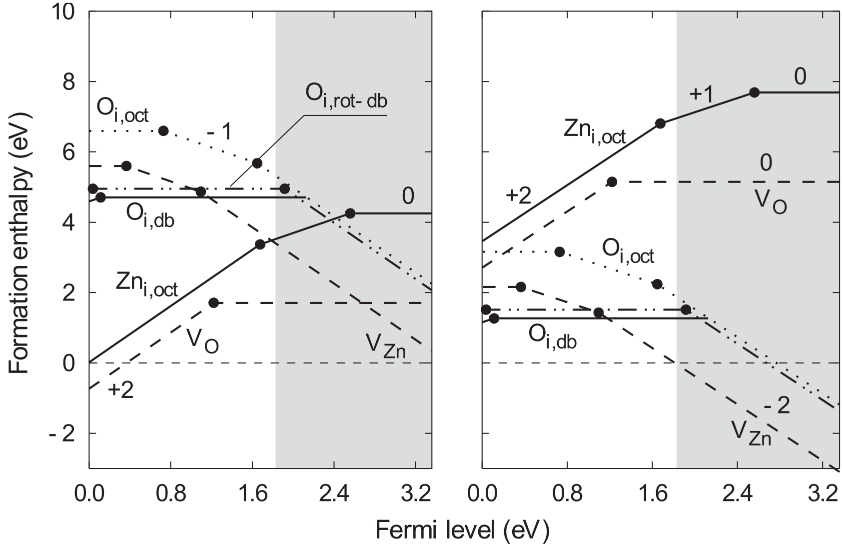

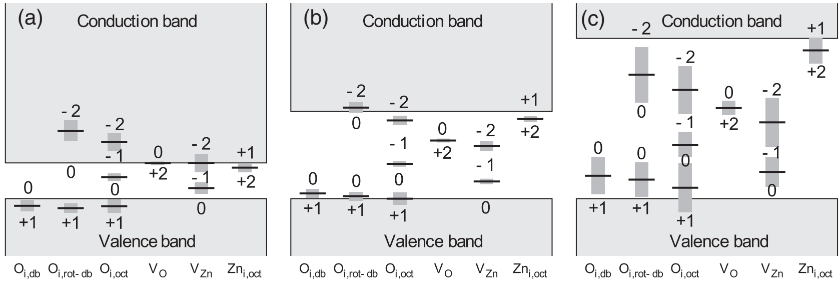

Fig. 1.13. *Top*: Variation of defect formation enthalpies with Fermi level under zinc- (*left*) and oxygen-rich (*right*) conditions as obtained from GGA+U calculations. The *gray shaded area* indicates the difference between the calculated and the experimental band gap. The *numbers* in the plot indicate the defect charge state; parallel lines imply equal charge states; *Bottom*: Transition levels in the band gap calculated within GGA (**a**), GGA+U (**b**) and using an extrapolation formula described in [115]. The *dark gray shaded areas* indicate error bars. Copyright (2006) by the American Physical Society

energy is two times the band gap. This is more than 6 eV and of the order of a typical defect formation enthalpy.

In recent years, there has been considerable effort to derive defect formation enthalpies of intrinsic defects in ZnO [108–110, 113–117]. An example is shown in Fig. 1.13 [115]. Horizontal curves belong to neutral defects, curves with positive or negative slopes to charged donors or acceptors, respectively. The donor with the lowest formation enthalpy is the oxygen vacancy V_O, the acceptor with the lowest formation enthalpy the zinc vacancy V_{Zn}.

This corresponds to a Frenkel type defect behavior. Negative defect formation enthalpies corresponds to unstable crystals (spontaneous defect formation) and indicate the limit for physically reasonable Fermi level positions.

Figure 1.13 includes the oxygen dumbbell interstitial or split interstitial defects ($O_{i,db}$ and $O_{i,rot-db}$). This particular defect was first mentioned by Lee et al. [113] and later treated extensively by Erhart and coworkers [114, 115]. The oxygen dumbbell interstitial corresponds to two oxygen atoms in the oxidation state −1, which occupy an oxygen lattice site. It can, therefore, also be considered as a peroxide-like defect. The atomic arrangement of the defects is shown in Fig. 1.14 together with the ideal lattice structure and the octahedral interstitial oxygen defect [114]. The oxygen dumbbell interstitial is an amphoteric defect, i.e., it behaves as a donor and as an acceptor. However, the transition energy for the donor is close to the valence band maximum, providing a very deep donor level. The transition energy for the acceptor is far above the valence band maximum, hence also providing a deep defect state. Although the dumbbell interstitial, therefore, does not contribute to the

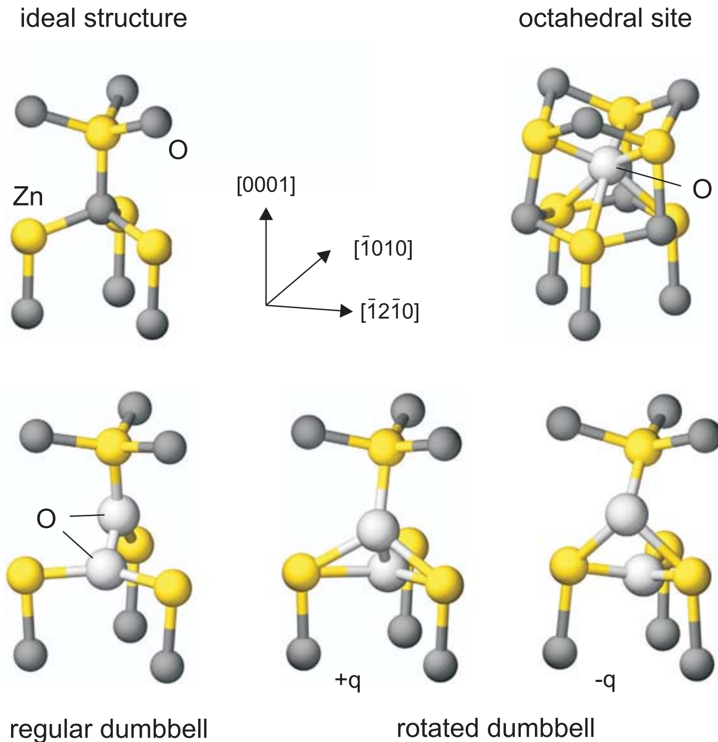

Fig. 1.14. Dumbbell oxygen interstitial defects in ZnO in comparison to the ideal lattice structure and the octahedral oxygen interstitial [114, 115]. The structure of the rotated dumbbell interstitial depends on the charge state. Copyright (2005) by the American Physical Society

electrical conductivity of ZnO, it is essential for describing oxygen diffusion in ZnO (see Sect. 1.6.2).

The defect transition energies are given in the lower part of Fig. 1.13. These are relevant for establishing the equilibrium Fermi level position and might help to explain the origin of the usually observed residual n-type conductivity of ZnO. Unfortunately, the band gaps calculated by density functional theory are typically much too low. Using the standard local density approximation (LDA) or the generalized gradient approximation (GGA), the band gap of ZnO is determined as 0.7–0.9 eV (see e.g., [115]). A larger, but still too small band gap of $\sim$1.8 eV is derived when a +U correction, which accounts for the self-interaction terms, is applied (see [115] and references therein). The literature on intrinsic defects in ZnO differs considerably with respect to the defect transition energies [108–110, 113–117]. A recent comparison of the different approaches is given in [115], where also a sophisticated interpolation scheme is proposed to overcome the band gap problem. The resulting defect transition energies are given in Fig. 1.13 (bottom right).

The lowering of the defect formation enthalpy with the movement of the Fermi energy leads to an increase of the defect concentration. Generally, donor (acceptor) doping leads to a rise (lowering) of the Fermi energy and therefore to a lowering of the formation enthalpy of intrinsic acceptors (donors). This mechanism leads to a limitation of the Fermi level movement and is called self-compensation [118–120]. It is well known for many semiconductors and leads to a limitation of the doping. In the extreme case of insulators, doping does not lead to creation of electrons or holes but only introduces compensating intrinsic defects [106, 107].

Doping limits in ZnO are important in two aspects: The possibility for p-type doping and the possibility for degenerate n-type doping. P-type conductivity requires a Fermi energy close to the valence band maximum, where the formation enthalpy of compensating donors is very low. According to defect calculations, the most important intrinsic defect for the compensation of p-type conductivity is the oxygen vacancy. On the other hand, the formation of zinc vacancies will limit n-type doping in ZnO. That this limitation occurs for Fermi level positions well above the conduction band minimum is a prerequisite for a transparent conducting electrode material, as otherwise no high electron concentrations are possible. However, it is indeed observed experimentally that the doping efficiency (number of free carriers per dopant atom) decreases with the increase of the dopant concentration [121] (see Chaps. 6 and 8).

The electron concentration in donor-doped TCOs becomes compensated with increasing oxygen partial pressure. The nature of the compensating defect thereby depends on the material. As mentioned earlier, compensation of n-type doping in ZnO occurs by introduction of zinc vacancies. In contrast, compensation in In_2O_3 is accomplished by oxygen interstitials [117]. Their importance in Sn-doped In_2O_3 has been already pointed out by Frank

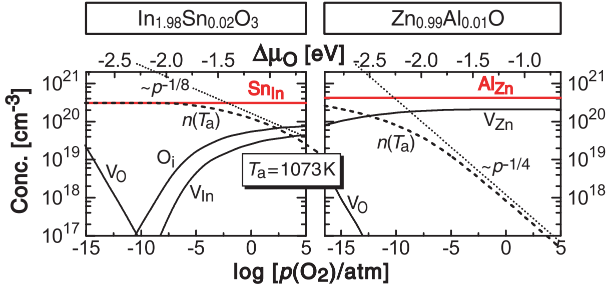

Fig. 1.15. Electron concentration (*dashed line*) of Sn-doped indium oxide and Al-doped ZnO in dependence on oxygen partial pressure for a dopant concentration of 1 % [117]. With increasing oxygen partial pressure the donors become compensated by oxygen interstitials (In_2O_3) or by zinc vacancies (ZnO). Reprinted with permission from [117]. Copyright (2007) by the American Physical Society

and Köstlin in 1982 [122]. The electron concentration for Al-doped ZnO and Sn-doped In_2O_3 in dependence on oxygen pressure has been calculated by Lany and Zunger [117]. The result is presented in Fig. 1.15. From Fig. 1.15, it is also evident that, in contrast to frequent assertions, oxygen vacancies are irrelevant for establishing the free carrier concentration in doped TCOs.

The defect structure described by Fig. 1.13 does not provide a straightforward explanation for the residual n-type conductivity [116,117,123]. First, the oxygen vacancy is a deep donor and cannot introduce enough carriers because of the large ionization energy. On the other hand, the zinc interstitial has a low ionization energy but a rather high formation enthalpy and is, therefore, not present in required amounts. This difficulty is explicitly treated by Lany and Zunger, who suggest a metastable oxygen vacancy defect induced by optical excitation as origin of the residual n-type conductivity [117, 123]. Alternatively, van de Walle has suggested that hydrogen, which forms a shallow donor in ZnO, causes the n-type conductivity [124] as also confirmed experimentally [10, 125–128] (See also Chap. 2).

1.6.2 Self-Diffusion in ZnO

Self-diffusion in materials occurs by repeated occupation of defects. Depending on the defects involved one can distinguish between (1) vacancy, (2) interstial, and (3) interstitialcy mechanisms [107]. As an example, different diffusion paths for oxygen interstitials are illustrated in Fig. 1.16 [129]. For a detailed description of diffusion paths for oxygen vacancies, zinc vacancies and zinc interstitials the reader is also referred to literature [129, 130].

When moving in a crystal, an atom has to surmount an energy barrier, which is called the migration enthalpy ΔH_m. The mobility of a diffusing species is, therefore, thermally activated and diffusion is described by the

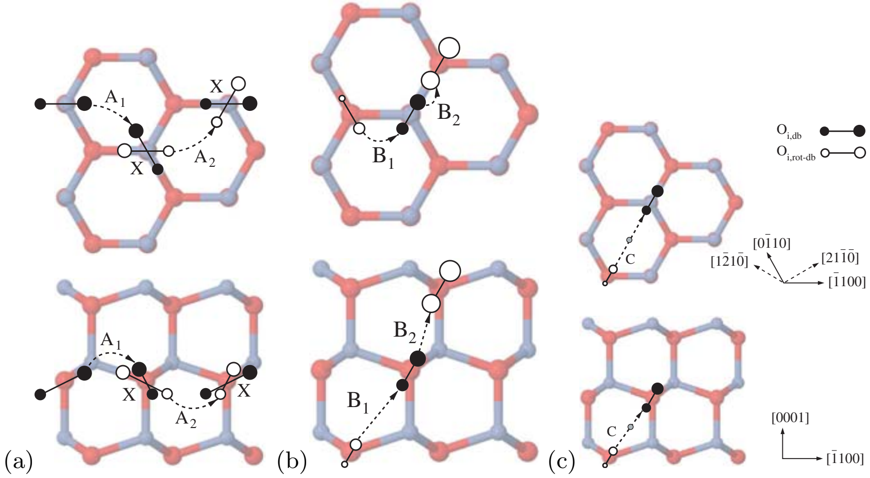

Fig. 1.16. Diffusion paths accessible to oxygen interstitials on the wurtzite lattice via jumps to first or second nearest neighbor sites [129]. Panels (**a**) and (**b**) show in-plane and out-of-plane diffusion paths to first nearest oxygen neighbors, panel (**c**) illustrates out-of-plane diffusion via second nearest oxygen neighbors. The size of the spheres scales with the position of the atom along the [0001] axis. Copyright (2006) by the American Physical Society

diffusion coefficient D given by a prefactor D_0 and an activation energy ΔH_m according to

$$D = D_0 \exp\left(-\Delta H_\mathrm{m}/k_\mathrm{B}\mathrm{T}\right) \tag{1.3}$$

However, the diffusivity also depends on the concentration of defects, which is also thermally activated according to (1.2). Hence, the self-diffusion coefficient D is described as

$$D \propto \exp\left(-\Delta H_\mathrm{d}/k_\mathrm{B}\mathrm{T}\right) \sum \exp\left(-\Delta H_\mathrm{m}/k_\mathrm{B}\mathrm{T}\right) \tag{1.4}$$

where the sum covers all possible diffusion paths. Since the defect formation enthalpy depends on the chemical potential and on the Fermi level position, the diffusivity will too. Furthermore, the dominant diffusion mechanism can change with chemical potential (oxygen partial pressure). This has been explicitly described for oxygen diffusion in ZnO by Erhart and Albe [129] where at low oxygen partial pressure a vacancy mechanism is prevalent while an interstitialcy mechanism dominates at higher oxygen partial pressures. In doped materials, the defect concentration can be constant over a range of temperatures and partial pressures [106,107]. Only in this case, the activation energy of diffusion is simply given by ΔH_m.

Diffusion of oxygen [131–136] and zinc [62, 131, 137–145] in ZnO (self-diffusion) has been investigated experimentally by a number of authors starting in the early 1950s (see also the review of experimental data in [129] for

oxygen and in [130] for zinc diffusion). However, no consistent picture has emerged from these studies. Erhart and Albe have calculated oxygen diffusion in ZnO using density functional theory [129, 130]. The advantage of this approach is that both defect concentrations and migration enthalpies can be determined. The calculation shows that the migration barriers for oxygen diffusion crucially depend on the charge state of the defects and, therefore, also on the Fermi energy position in the gap, which is determined by extrinsic doping and intrinsic defects. Lowest migration barriers for oxygen are obtained by diffusion employing the dumbbell and the rotated dumbbell interstitials, which highlights the importance of these kinds of defects. Figure 1.17 shows the calculated diffusivity of oxygen in ZnO in dependence on the chemical potential and Fermi energy position in the gap at $T = 1\,300\,\mathrm{K}$ (top). At the bottom, the calculated temperature dependence of the diffusivity for cases where either the vacancy mechanism or the interstitialcy mechanism dominate is shown in comparison to compiled experimental data. Except for the older data points, which are probably subject to an experimental artifact (see discussion in [129] and [134]), all experimental values are well reproduced by the calculation.

Erhart and Albe also calculated zinc diffusion in ZnO [130]. The results are displayed in Fig. 1.18 together with a comparison to experimental data. Depending on chemical potential and Fermi level position either zinc vacancy or zinc interstitial diffusion can dominate. In the case of n-type material, where the Fermi level is close to the conduction band, zinc diffusion is mostly accomplished via the vacancy mechanism.

The diffusivities of Zn are generally larger than those of oxygen. Following the calculations, the diffusivities in ZnO can be ordered according to $\mathrm{Zn_i} > \mathrm{O_i} > \mathrm{V_{Zn}} > \mathrm{V_O}$ [130]. In particular, the migration barriers are very small (0.2–0.4 eV) for zinc interstitials [130]. The small migration barriers lead to an onset of migration already at temperatures of $\sim$100 K, which explains the remarkably high radiation hardness of ZnO caused by the annealing of defects at rather low temperatures [146–148].

1.7 Applications of ZnO

Zinc oxide is a very old technological material. Already in the Bronze Age it was produced as a byproduct of copper ore smelting and used for healing of wounds. Early in history it was also used for the production of brass (Cu–Zn alloy). This was the major application of ZnO for many centuries before metallic zinc replaced the oxide [149]. With the start of the industrial age in the middle of the nineteenth century, ZnO was used in white paints (chinese white), in rubber for the activation of the vulcanization process and in porcelain enamels. In the following a number of existing and emerging electronic applications of ZnO are briefly described.

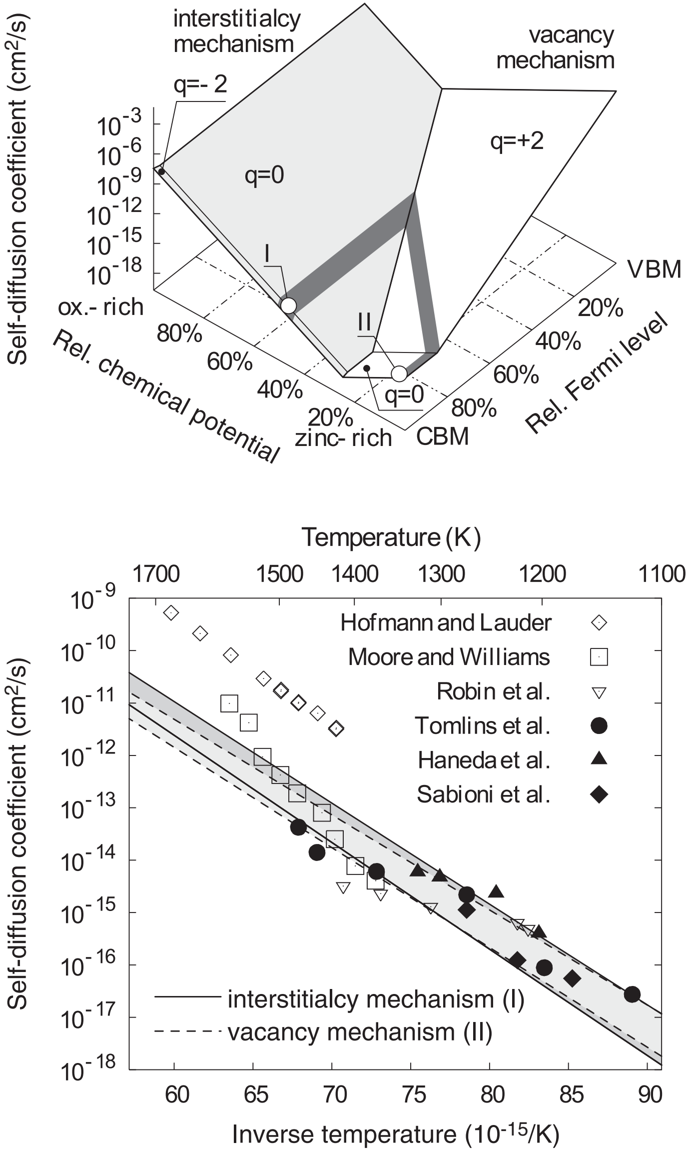

Fig. 1.17. Oxygen diffusion in ZnO [129]. *Top*: Dependence of diffusivity on chemical potential and Fermi level at a temperature of 1 300 K illustrating the competition between vacancy and interstitialcy mechanisms. The *dark grey* areas indicate the experimental data range around 1 300 K. *Bottom*: Comparison between calculation and experiment. Experimental data from Moore and Williams [131], Hofmann and Lauder [132], Robin et al. [133], Tomlins et al. [134], Haneda et al. [135], and Sabioni et al. [136]. *Solid* and *dashed lines* correspond to regions I (interstitialcy mechanism dominant) and II (vacancy mechanism dominant) in the *top graph*, respectively. Copyright (2006) by the American Physical Society

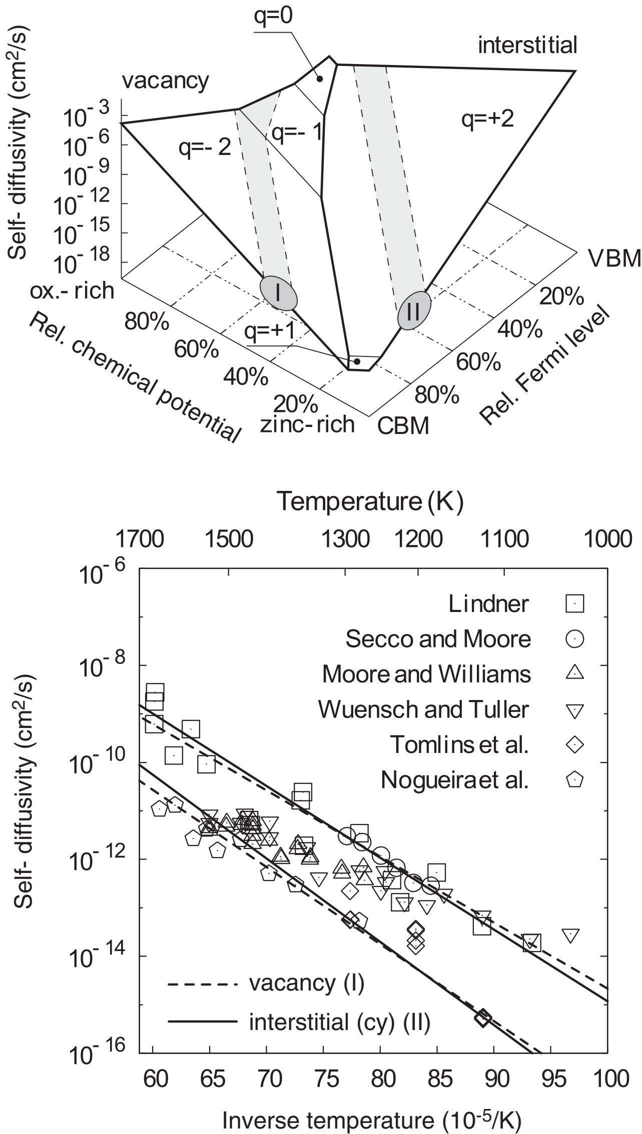

Fig. 1.18. Zinc diffusion in ZnO [130]. *Top*: Dependence of diffusivity on chemical potential and Fermi level at a temperature of 1 300 K illustrating the competition between vacancy and interstitial mechanisms. The *shaded grey areas* indicate the ranges selected for comparison with experimental data. *Bottom*: Comparison between calculation and experiment. Experimental data from Lindner [137], Secco and Moore [138,139], Moore and Williams [131], Wuensch and Tuller [143], Tomlins et al. [62], and Nogueira et al. [144, 145]. *Solid* and *dashed lines* correspond to regions I (vacancy mechanism) and II (interstitial(cy) mechanism) in the *top graph*, respectively. Reprinted with permission from [130]. Copyright (2006), American Institute of Physics

1.7.1 Transparent Electrodes

Thin film solar cells need a transparent window electrode for light transmission and extraction of the photocurrent. Currently used configurations for thin film solar cells are schematically shown in Fig. 1.19. Highly-doped ZnO films are used particularly in amorphous silicon [150] and Cu(In,Ga)$(S,Se)_2$ [151, 152] cells. High doping levels with carrier concentrations up to $1.5 \times 10^{21}\,cm^{-3}$ and resistivities as low as $2 \times 10^{-4}\,\Omega\,cm$ are achieved by addition of trivalent dopants like boron, aluminium, or gallium. For amorphous silicon cells, the degenerately n-doped transparent electrode forms a tunnel junction to a highly p- or n-doped material. In Cu(In,Ga)$(S,Se)_2$ cells ZnO is a part of the electric p/n junction. To obtain high efficiencies, a bilayer structure of a thin ($\sim$50 nm) nominally undoped ZnO and a highly n-doped layer is typically used. The main advantage of zinc oxide is that it is much cheaper than indium oxide, a prerequisite for large area technologies like thin film solar cells. The role of ZnO in amorphous silicon and Cu(In,Ga)$(S,Se)_2$ thin film solar cells is discussed in detail in Chaps. 4, 6, 8, and 9.

In display technology mostly ITO (Sn-doped In_2O_3) is used today. However, because of the limited availability of In, there is a strong interest in replacing ITO by other materials. The advantages of ITO compared with other transparent conducting oxides are the still higher conductivities, the possibility to prepare very flat films and the good etching behavior, which enables highly reproducible structure formation. Today, most flat panel

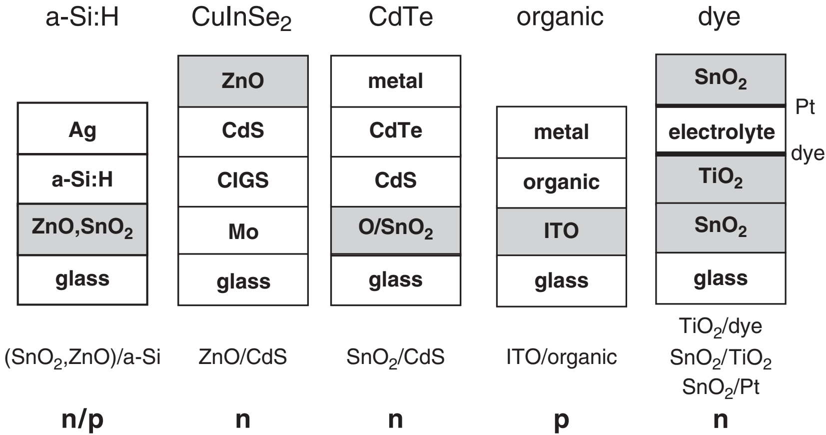

Fig. 1.19. Transparent conducting oxide electrodes in different types of thin film solar cells. TCO contacts are given at the bottom of each structure. The bottom most row indicates the doping type of the semiconductor, which is in contact to the TCO

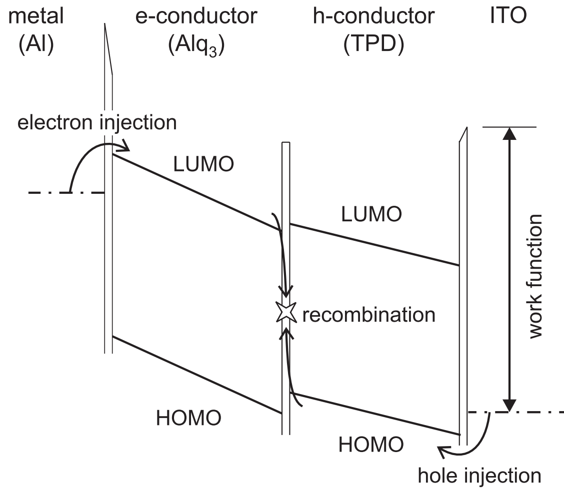

Fig. 1.20. Schematic energy band diagram of a two-layer organic light emitting diode (OLED), in which tin-doped indium oxide (ITO) is used to inject holes into the highest occupied molecular orbital (HOMO) and a low work function metal to inject electrons into the lowest unoccupied molecular orbital (LUMO)

displays are using LCD[4] technology [153]. In these applications, the interface between the transparent electrode and the polymer layer inserted for orientation of the liquid crystals does not have an active electronic function in the device; i.e., it is simply used to transmit light and to apply an electric field for reorientation of the crystals.

The situation is different in organic light emitting devices (OLED), where ITO is almost exclusively used as anode material [154]. A schematic layout together with an energy band diagram of an OLED is displayed in Fig. 1.20. In OLEDs, ITO is used to inject holes into the organic conductor. Typically an oxidizing surface treatment is performed prior to the deposition of the organic material [155–157]. These lead to an increase of the work function, which is believed to reduce the hole injection barrier. ZnO has also been tested as electrode material in OLEDs [158, 159].

1.7.2 Varistors

Varistors are voltage-dependent resistors, which are extensively used for overvoltage protection [160]. Their size varies from a few millimeters on printed electronic circuit boards for low voltage operation to more than 1 m for high voltage operation in electrical power grids. The latter are made by a stack of individual resistors of up to 10 cm diameter. ZnO varistors were first developed by Matsuoka in Japan at the beginning of the 1970s [161]. They

[4] Liquid crystal display.

are made from sintered polycrystalline ceramics using different additives as Bi_2O_3, Sb_2O_3, or other metal oxides. The material is poorly doped and the additives segregate to the grain boundaries during sintering leading to a large barrier for electron transport [162,163]. More details on the function and the properties of ZnO varistors are described in Chap. 2.

1.7.3 Piezoelectric Devices

There are several applications of ZnO that are due to its excellent piezoelectric properties [28,164]. Examples are surface-acoustic wave (SAW) devices and piezoelectric sensors [28,165–167]. Typically, SAW devices are used as band pass filters in the tele-communications industry, primarily in mobile phones and base stations. Emerging field for SAW devices are sensors in automotive applications (torque and pressure sensors), medical applications (chemical sensors), and other industrial applications (vapor, humidity, temperature, and mass sensors). Advantages of acoustic wave sensors are low costs, ruggedness, and a high sensitivity. Some sensors can even be interrogated wirelessly, i.e., such sensors do not require a power source.

In an SAW device, a mechanical deformation is induced by electrical contact fingers in a nearly isolating, highly (0001)-textured ZnO film (see insert in Fig. 1.21). The insulating wave travels along the ZnO film surface with the velocity of sound in ZnO and is detected at the end of the device by another metal–finger contact. High-frequency electrical signals (10 MHz–10 GHz) can be transformed to SAWs with typical wave velocities of about $3\,\mathrm{km\,s^{-1}}$. Because of the much lower acoustic velocity, compared with the velocity of light, such SAW devices can also be used as acoustic delay lines with a characteristic frequency dependence suitable for high-frequency filters. A typical frequency curve of an SAW device is shown in Fig. 1.21.

1.7.4 Phosphors

In displays ZnO powders are used as green phosphors [169]. Recently, magnetron sputtered films of ZnO-based compounds, for instance Zn_2SiO_4:Mn or $ZnGa_2O_4$:Mn were used as green phosphors in thin-film electroluminescence displays [170,171]. Even white cathodoluminescence was observed for self-assembled ZnO micropatterns [172].

1.7.5 Transparent Oxide Thin Film Transistors

Recently, field-effect transistors based on zinc oxide were reported [173,174], opening the opportunity to design microelectronic devices that are transparent and/or work at high temperatures [175]. More details on thin film transistors employing transparent conducting oxides are given in Chap. 2.

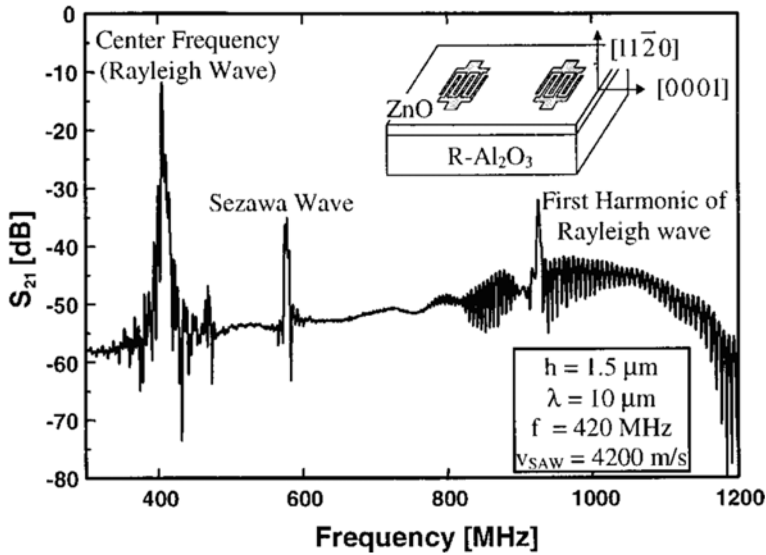

Fig. 1.21. Frequency spectrum of a 10 μm wavelength SAW device on a 1.5 μm thick ZnO film on an r-sapphire substrate. The ZnO film was deposited by MOCVD using diethyl-zinc and oxygen. The inset shows the geometry of the device with the interdigitated contact fingers. Reprinted with permission from [168]

1.7.6 Spintronics

Another prospective application of zinc oxide is the alloying with magnetic atoms like manganese, cobalt, or nickel to prepare diluted magnetic semiconducting alloys that are interesting as materials for spintronics, promising the possibility to use the spin of the electrons for electronic devices [176].

Acknowledgement. The authors are grateful to Paul Erhart and Karsten Albe for extensive discussions of the defect properties of ZnO and for the supply of original versions of their figures.

References

1. J. Bardeen, W.H. Brattain, Phys. Rev. **74**, 230 (1948)
2. A.R. Hutson, Phys. Rev. Lett. **4**, 505 (1960)
3. F.S. Hickernell, Proc. IEEE **64**, 631 (1976)
4. C. Klingshirn, H. Priller, M. Decker, J. Brückner, H. Kalt, R. Hauschild, J. Zeller, A. Waag, A. Bakin, H. Wehmann, K. Thonke, R. Sauer, R. Kling, F. Reuss, C. Kirchner, Adv. Solid State Phys. **45**, 275 (2005)
5. C. Klingshirn, M. Grundmann, A. Hoffmann, B. Meyer, A. Waag, Phys. J. **5**, 33 (2006)

6. G. Heiland, E. Mollwo, F. Stöckmann, Solid State Phys. **8**, 191 (1959)
7. W. Hirschwald, in *Current Topics in Material Science*, vol. 7, ed. by E. Kaldis (North-Holland, Amsterdam, 1981), pp. 144–482
8. C. Klingshirn, H. Haug, Phys. Rep. **70**, 315 (1981)
9. U. Özgür, Y.I. Alivov, C. Liu, A. Teke, M.A. Reshchikov, S. Dogan, V. Avrutin, S.J. Cho, H. Morkoc, J. Appl. Phys. **98**, 041301 (2005)
10. N.H. Nickel, E. Terukov (eds.), *Zinc Oxide-A Material for Micro- and Optoelectronic Applications* (Springer, Dordrecht, 2005)
11. C. Jagadish, S.J. Pearton (eds.), *Zinc Oxide: Bulk, Thin Films and Nanostructures* (Elsevier, Oxford, 2006)
12. K. Nomura, H. Ohta, K. Ueda, T. Kamiya, M. Hirano, H. Hosono, Science **300**, 1269 (2003)
13. D.C. Look, Semicond. Sci. Technol. **20**, S55 (2005)
14. B.K. Meyer, J. Sann, A. Zeuner, Adv. Solid State Phys. **45**, 289 (2005)
15. B. Claflin, D.C. Look, S.J. Park, G. Cantwell, J. Cryst. Growth **287**, 16 (2006)
16. R.G.W. Wyckoff, *Crystal Structures* (Interscience, New York, 1963)
17. A.N. Mariano, R.E. Hanneman, J. Appl. Phys. **34**, 384 (1963)
18. http://minerals.usgs.gov/minerals/pubs/commodity/zinc/
19. W.L. Bragg, Phil. Mag. **39**, 647 (1920)
20. F. Decremps, J. Zhang, R.C. Lieberman, Europhys. Lett. **51**, 268 (2000)
21. S. Desgreniers, Phys. Rev. B **58**, 14102 (1998)
22. A. Dargys, J. Kundrotas, *Handbook of Physical Properties of Ge, Si, GaAs and InP* (Science Encycl. Publ., Vilnius, 1994)
23. O. Madelung (ed.), *Semiconductors Basic Data* (2nd ed.) (Springer Verlag, Berlin, 1996)
24. H.L. Hartnagel, A.L. Dawar, A.K. Jain, C. Jagadish, *Semiconducting Transparent Thin Films* (Institute of Physics Publishing, Bristol, 1995)
25. A.A. Khan, Acta Cryst. A **24**, 403 (1968)
26. R.R. Reeber, J. Appl. Phys. **41**, 5063 (1970)
27. S. Adachi, *Properties of Group IV, III-V and II-VI Semiconductors* (John Wiley & Sons, West Sussex, England, 2005)
28. Y. Lu, N.W. Emanetoglu, Y. Cheng, in *Zinc Oxide. Bulk, Thin films and Nanostructures*, ed. by C. Jagadish, S.J. Pearton (Elsevier, Oxford, 2006), pp. 443–489
29. R. Helbig (ed.), *Landolt Börnstein, New Series III/17d; II-VI and I-VII Compounds* (Springer, Berlin Heidelberg Newyork, 1984)
30. I. Hamberg, C.G. Granqvist, J. Appl. Phys. **60**, R123 (1986)
31. H. Fujiwara, M. Kondo, Phys. Rev. B **71**, 075109 (2005)
32. M. Chase, *JANAF Thermochemical Tables*, 4th edn. J. Phys. Chem. Ref. Data, Monograph 9 (NIST, 1998)
33. D.S. Ginley, C. Bright, MRS Bull. **25**(Aug), 15 (2000)
34. T. Minami, Semicond. Sci. Technol. **20**, S35 (2005)
35. R.L. Weiher, R.P. Ley, J. Appl. Phys. **37**, 299 (1966)
36. I. Hamberg, C.G. Granqvist, K.F. Berggren, B.E. Sernelius, L. Engström, Phys. Rev. B **30**, 3240 (1984)
37. Y. Gassenbauer, R. Schafranek, A. Klein, S. Zafeiratos, M. Hävecker, A. Knop-Gericke, R. Schlögl, Phys. Rev. B **73**, 245312 (2006)
38. S.P. Harvey, T.O. Mason, Y. Gassenbauer, R. Schafranek, A. Klein, J. Phys. D: Appl. Phys. **39**, 3959 (2006)

39. P. Erhart, A. Klein, R.G. Egdell, K. Albe, Phys. Rev. B **75**, 153205 (2007)
40. K. Bädeker, Ann. Phys. (Leipzig) **22**, 749 (1907)
41. T.O. Mason, D.R. Kammler, B.J. Ingram, G.B. Gonzalez, D.L. Young, T.J. b. Coutts, Thin Solid Films **445**, 186 (2003)
42. F.P. Koffyberg, Phys. Rev. B **13**, 4470 (1976)
43. C. McGuinness, C.B. Stagarescu, P.J. Ryan, J.E. Downes, D. Fu, K.E. Smith, R.G. Egdell, Phys. Rev. B **68**, 165104 (2003)
44. Z. Zhao, D.L. Morel, C.S. Ferekides, Thin Solid Films **413**, 203 (2002)
45. A.J. Freeman, K.R. Poeppelmeier, T.O. Mason, R.P.H. Chang, T.J. Marks, MRS Bull. **25**(Aug), 45 (2000)
46. T. Minami, MRS Bull. **25**(Aug), 38 (2000)
47. H. Kawazoe, M. Yasukawa, H. Hyodo, M. Kurita, H. Yanagi, H. Hosono, Nature **389**, 939 (1997)
48. A. Kudo, H. Yanagi, H. Hosono, H. Kawazoe, Appl. Phys. Lett. **73**, 220 (1998)
49. H. Kawazoe, H. Yanagi, K. Ueda, H. Hosono, MRS Bull. **25**(Aug), 28 (2000)
50. K. Ueda, S. Inoue, S. Hirose, H. Kawazoe, H. Hosono, Appl. Phys. Lett. **77**, 2701 (2000)
51. H. Yanagi, T. Hase, S. Ibuki, K. Ueda, H. Hosono, Appl. Phys. Lett. **78**, 1583 (2001)
52. H. Yanagi, K. Ueda, H. Ohta, M. Orita, M. Hirano, H. Hosono, Solid State Commun. **121**, 15 (2001)
53. H. Yanagi, J. Tate, S. Park, C.H. Park, D.A. Keszler, Appl. Phys. Lett. **82**, 2814 (2003)
54. B.J. Ingram, T.O. Mason, R. Asahi, K.T. Park, A.J. Freeman, Phys. Rev. B **64**, 155114 (2001)
55. B.J. Ingram, B.J. Harder, N.W. Hrabe, T.O. Mason, Chem. Mater. **16**, 5623 (2004)
56. X. Nie, S.H. Wei, S.B. Zhang, Phys. Rev. Lett. **88**, 066405 (2002)
57. R. Helbig, J. Cryst. Growth **15**, 25 (1972)
58. T.B. Massalski, H. Okamoto, P.R. Subramanian, L. Kacprzak (eds.), *Binary Alloy Phase Diagrams,* Vol. 3 (ASM International, Materials Park, Ohio, 1990)
59. N.G. Vannerberg, Ark. Kemi **14**, 119 (1959)
60. D.F. Anthrop, A.W. Searcy, J. Phys. Chem. **68**, 2335 (1964)
61. K.I. Hagemark, P.E. Toren, J. Electrochem. Soc. **122**, 992 (1975)
62. G.W. Tomlins, J.L. Routbort, T.O. Mason, J. Appl. Phys. **87**, 117 (2000)
63. K. Lott, S. Shinkarenko, T. Kirsanova, L. Türn, E. Gorohova, A. Grebennik, A. Vishnjakov, Phys. Stat. Sol. (c) **1**, 2237 (2004)
64. O. Fritsch, Ann. Phys. **[5], 22**, 375 (1935)
65. D. Rykl, J. Bauer, Kristall und Technik **3**, 375 (1968)
66. K. Maeda, M. Sato, I. Niikura, T. Fukuda, Semicond. Sci. Technol. **20**, S49 (2005)
67. G. Bogner, E. Mollwo, J. Phys. Chem. Solids **6**, 136 (1958)
68. M. Hirose, Y. Furuya, I. Kubo, Jpn. J. Appl. Phys. **9**, 726 (1970)
69. D.F. Bliss, in *Encyclopedia of Materials: Science and Technology*, vol. 10, ed. by K.H.J. Buschow, R. Cahn, M. Flemings, B. Ilschner, E. Kramer, S. Mahajan (Elsevier, Oxford, 2001), pp. 9888–9891
70. J. Nause, B. Nemeth, Semicond. Sci. Technol. **20**, S45 (2005)
71. D. Schulz, S. Ganschow, D. Klimm, M. Neubert, M. Roßberg, M. Schmidbauer, R. Fornari, J. Cryst. Growth **296**, 27 (2006)

72. D.C. Look, D.C. Reynolds, J.R. Sizelove, R.L. Jones, C.W. Litton, G. Cantwell, W.C. Harsch, Solid State Commun. **105**, 399 (1998)
73. E.V. Kortunova, P.P. Chvanski, N.G. Nikolaeva, J. Phys. IV France **126**, 39 (2005)
74. K. Ellmer, J. Phys. D: Appl. Phys. **33**, R17 (2000)
75. J.R. Bellingham, W.A. Phillips, C.J. Adkins, J. Phys.: Cond. Mat. **2**, 6207 (1990)
76. P. Kuppusami, G. Vollweiler, D. Rafaja, K. Ellmer, Appl. Phys. A **81**, 183 (2005)
77. E. Scharowsky, Z. Phys. **135**, 318 (1953)
78. K. Yamada, S. Tobisawa, J. Appl. Phys. **66**, 5309 (1989)
79. J. Tornow, K. Schwarzburg, J. Phys. Chem. C 111, 8692 (2007)
80. M.H. Huang, Y. Wu, H. Feick, N. Tran, E. Weber, P. Yang, Adv. Mater. **13**, 113 (2001)
81. R.B. Peterson, C.L. Fields, B.A. Gregg, Langmuir **20**, 5114 (2004)
82. L. Wischmeier, T. Voss, S. Brner, W. Schade, Appl. Phys. A **84**, 111 (2006)
83. G.C. Yi, V. Wang, W.I. Park, Semicond. Sci. Technol. **20**, S22 (2005)
84. M. Huang, S. Mao, H. Feick, H. Yan, Y. Wu, H. Kind, E. Weber, R. Russo, P. Yang, Science **292**, 1897 (2001)
85. Y.W. Heo, F. Ren, D.P. Norton, in *Zinc Oxide: Bulk, Thin Films and Nanostructures*, ed. by C. Jagadish, S. Pearton (Elsevier, Oxford, 2006), pp. 491–523
86. T. Soga (ed.), *Nanostructured Materials for Solar Energy Conversion* (Elsevier, Oxford, 2006)
87. M.S. White, D.C. Olson, S.E. Shaheen, N. Kopidakis, D.S. Ginley, Appl. Phys. Lett. **89**, 143517 (2006)
88. X. Wang, J. Song, J. Liu, Z.L. Wang, Science **316**, 102 (2007)
89. W.A. Harrison, *Electronic Structure and the Properties of Solids* (Dover Publications, New York, 1989)
90. P.Y. Yu, M. Cardona, *Fundamentals of Semiconductors. Physics and Materials Properties*, 3rd edn. (Springer, Berlin Heidelberg Newyork, 2001)
91. J.L. Shay, J.H. Wernick, *Ternary Chalcopyrite Semiconductors* (Pergamon, Oxford, 1975)
92. B.K. Meyer, H. Alves, D.M. Hofmann, W. Kriegseis, D. Forster, F. Bertram, J. Christen, A. Hoffmann, M. Straßburg, M. Dworzak, U. Haboeck, A.V. Rodina, Phys. Stat. Sol. (a) **241**, 231 (2004)
93. J.E. Jaffe, A. Zunger, Phys. Rev. B **29**, 1882 (1984)
94. S.H. Wei, A. Zunger, Phys. Rev. B **37**, 8958 (1988)
95. S.H. Wei, A. Zunger, Appl. Phys. Lett. **72**, 2011 (1998)
96. D. Vogel, P. Krüger, J. Pollmann, Phys. Rev. B **52**, R14316 (1995)
97. D. Vogel, P. Krüger, J. Pollmann, Phys. Rev. B **54**, 5495 (1996)
98. C.L. Dong, C. Persson, L. Vayssieres, A. Augustsson, T. Schmitt, M. Mattesini, R. Ahuja, C.L. Chang, J.H. Guo, Phys. Rev. B **70**, 195325 (2004)
99. A. Ohtomo, M. Kawasaki, T. Koida, K. Masubuchi, H. Koinuma, Y. Sakurai, Y. Yoshida, T. Yasuda, Y. Segawa, Appl. Phys. Lett. **72**, 2466 (1998)
100. A. Ohtomo, M. Kawasaki, I. Ohkubo, H. Koinuma, T. Yasuda, Y. Segawa, Appl. Phys. Lett. **75**, 980 (1999)
101. T. Makino, Y. Segawa, M. Kawasaki, A. Ohtomo, R. Shiroki, K. Tamura, T. Yasuda, H. Koinuma, Appl. Phys. Lett. **78**, 1237 (2001)

102. S. Choopun, R.D. Vispute, W. Yang, R.P. Sharma, T. Venkatesan, Appl. Phys. Lett. **80**, 1529 (2002)
103. R. Schmidt, B. Rheinländer, M. Schubert, D. Spemann, T. Butz, J. Lenzner, E.M. Kaidashev, M. Lorenz, A. Rahm, H.C. Semmelhack, M. Grundmann, Appl. Phys. Lett. **82**, 2260 (2003)
104. R. Schmidt-Grund, M. Schubert, B. Rheinländer, D. Fritsch, H. Schmidt, E.M. Kaidashev, C.M. Herzinger, M. Grundmann, Thin Solid Films **455–456**, 500 (2004)
105. G.V. Rao, F. Säuberlich, A. Klein, Appl. Phys. Lett. **87**, 032101 (2005)
106. F.A. Kröger, *The Chemistry of Imperfect Crystals* (North-Holland, Amsterdam, 1964)
107. J. Maier, *Physical Chemistry of Ionic Materials* (Wiley-VCH, Weinheim, 2004)
108. A.F. Kohan, G. Ceder, D. Morgan, C.G. van de Walle, Phys. Rev. B **61**, 15019 (2000)
109. S.B. Zhang, S.H. Wei, A. Zunger, Phys. Rev. B **63**, 075205 (2001)
110. F. Oba, S.R. Nishitani, S. Isotani, H. Adachi, I. Tanaka, J. Appl. Phys. **90**, 824 (2001)
111. H. Overhof, J.M. Spaeth, Phys. Rev. B **72**, 115205 (2005)
112. S.B. Zhang, J.E. Northrup, Phys. Rev. Lett. **67**, 2339 (1991)
113. E.C. Lee, Y.S. Kim, Y.G. Jin, K.J. Chang, Phys. Rev. B **64**, 085120 (2001)
114. P. Erhart, A. Klein, K. Albe, Phys. Rev. B **72**, 085213 (2005)
115. P. Erhart, K. Albe, A. Klein, Phys. Rev. B **73**, 205203 (2006)
116. A. Janotti, C.G. van de Walle, J. Cryst. Growth **287**, 58 (2006)
117. S. Lany, A. Zunger, Phys. Rev. Lett. **98**, 045501 (2007)
118. W. Walukiewicz, Physica B **302–303**, 123 (2001)
119. S.B. Zhang, S.H. Wei, A. Zunger, J. Appl. Phys. **83**, 3192 (1998)
120. J.A. van Vechten, J.D. Zook, R.D. Horning, B. Goldenberg, Jpn. J. Appl. Phys. **31**, 3662 (1992)
121. C. Agashe, O. Kluth, J. Hüpkes, U. Zastrow, B. Rech, M. Wuttig, J. Appl. Phys. **95**, 1911 (2004)
122. G. Frank, H. Köstlin, Appl. Phys. A **27**, 197 (1982)
123. S. Lany, A. Zunger, Phys. Rev. B **72**, 035215 (2005)
124. C.G. van de Walle, Phys. Rev. Lett. **85**, 1012 (2000)
125. S.F.J. Cox, E.A. Davis, S.P. Cottrell, P.J.C. King, J.S. Lord, J.M. Gil, H.V. Alberto, R.C. Vilo, J.P. Duarte, N.A. de Campos, A. Weidinger, R.L. Lichti, S.J.C. Irvine, Phys. Rev. Lett. **86**, 2601 (2001)
126. H. Moormann, D. Kohl, G. Heiland, Surf. Sci. **100**, 302 (1980)
127. L.Y. Chen, W.H. Chen, J.J. Wang, F.C.N. Hong, Y.K. Su, Appl. Phys. Lett. **85**, 5628 (2004)
128. G.A. Shi, M. Saboktakin, M. Stavola, S.J. Pearton, Appl. Phys. Lett. **85**, 5601 (2004)
129. P. Erhart, K. Albe, Phys. Rev. B **73**, 115207 (2006)
130. P. Erhart, K. Albe, Appl. Phys. Lett. **88**, 201918 (2006)
131. W.J. Moore, E.L. Williams, Discuss. Faraday Soc. **28**, 86 (1959)
132. J.W. Hoffman, I. Lauder, Trans. Faraday Soc. **66**, 2346 (1970)
133. R. Robin, A.R. Cooper, A.H. Heuer, J. Appl. Phys. **44**, 3770 (1973)
134. G.W. Tomlins, J.L. Routbort, T.O. Mason, J. Am. Ceram. Soc. **81**, 869 (1998)
135. H. Haneda, I. Sakaguchi, A. Watanabe, T. Ishigaki, J. Tanaka, J. Electroceram. **4**, 41 (1999)

136. A.C.S. Sabioni, M.J.F. Ramos, W.B. Ferraz, Mater. Res. **6**, 173 (2003)
137. R. Lindner, Acta Chem. Scand. **6**, 457 (1952)
138. E.A. Secco, W.J. Moore, J. Chem. Phys. **23**, 1170 (1955)
139. E.A. Secco, W.J. Moore, J. Chem. Phys. **26**, 942 (1957)
140. D.G. Thomas, J. Phys. Chem. Solids **3**, 229 (1957)
141. J.P. Roberts, C. Wheeler, Phil. Mag. **2**, 708 (1957)
142. J.P. Roberts, C. Wheeler, Trans. Faraday Soc. **56**, 570 (1960)
143. B.J. Wuensch, H.L. Tuller, J. Phys. Chem. Solids **55**, 975 (1994)
144. M.A. Nogueira, W.B. Ferraz, A.C.S. Sabioni, Mater. Res. **6**, 167 (2003)
145. M.A.N. Nogueira, A.C.S. Sabioni, W.B. Ferraz, Defect Diffus. Forum **237–240**, 163 (2005)
146. C. Coskun, D.C. Look, G.C. Farlow, J.R. Sizelove, Semicond. Sci. Technol. **19**, 752 (2004)
147. Y.V. Gorelkinskii, G.D. Watkins, Phys. Rev. B **69**, 115212 (2004)
148. K. Lorenz, E. Alves, E. Wendler, O. Bilani, W. Wesch, M. Hayes, Appl. Phys. Lett. **87**, 191904 (2005)
149. H.E. Brown, *Zinc Oxide. Properties and Applications* (Int. Lead Zinc Research Org., New York, 1976)
150. B. Rech, H. Wagner, Appl. Phys. A **69**, 155 (1999)
151. K. Ramanathan, M.A. Contreras, C.L. Perkins, S. Asher, F.S. Hasoon, J. Keane, D. Young, M. Romero, W. Metzger, R. Noufi, J. Ward, A. Duda, Progr. Photovolt.: Res. Appl. **11**, 225 (2003)
152. R. Klenk, J. Klaer, R. Scheer, M.C. Lux-Steiner, I. Luck, N. Meyer, U. Rühle, Thin Solid Films **480–481**, 509 (2005)
153. M. Katayama, Thin Solid Films **341**, 140 (1999)
154. L.S. Hung, C.H. Chen, Mater. Sci. Eng. R **39**, 143 (2002)
155. T. Kugler, W.R. Salaneck, H. Rost, A.B. Holmes, Chem. Phys. Lett. **310**, 391 (1999)
156. K. Sugiyama, H. Ishii, Y. Ouchi, K. Seki, J. Appl. Phys. **87**, 295 (2000)
157. Y. Gassenbauer, A. Klein, J. Phys. Chem. B **110**, 4793 (2006)
158. X. Jiang, F.L. Wong, M.K. Fung, S.T. Lee, Appl. Phys. Lett. **83**, 1875 (2003)
159. S.H.K. Park, J.I. Lee, C.S. Hwang, H.Y. Chu, Jpn. J. Appl. Phys. **44**, L242 (2005)
160. L.M. Levinson, H.R. Philipp, Ceram. Bull. **65**, 639 (1986)
161. M. Matsuoka, Jpn. J. Appl. Phys. **10**, 736 (1971)
162. M. Rossinelli, G. Blatter, F. Greuter, in *Electrical Ceramics*, vol. 36, ed. by B.C.H. Steele (Inst. of Ceramics, Shelton, 1985), pp. 1–17
163. G. Blatter, F. Greuter, Phys. Rev. B **34**, 8555 (1986)
164. A. Ballato, in *IEEE Ultrasonics Symposium Proceedings* (1996), pp. 575–583
165. B. Drafts, Sensors **17**(October), 68 (2000)
166. J.W. Grate, S.J. Martin, R.W. White, Analyt. Chem. **65**, 940 (1993)
167. J.W. Grate, S.J. Martin, R.W. White, Analyt. Chem. **65**, 987 (1993)
168. C. Gorla, N.W. Emanetoglu, S. Liang, W.E. Mayo, H.S. Y. Yu, M. Wraback, J. Appl. Phys. **85**, 2595 (1999)
169. K. Vanheusdalen, C.H. Seager, W.L. Warren, D.R. Tallant, J.A. Voigt, Appl. Phys. Lett. **68**, 403 (1996)
170. A.H. Kitai, Thin Solid Films **445**, 367 (2003)
171. T. Miyata, Y. Mochizuki, T. Minami, IEICE Trans. Electron. **E88-C**, 2065 (2005)

172. N. Saito, H. Haneda, T. Sekiguchi, N. Ohashi, I. Sakaguchi, K. Koumoto, Adv. Mater. **14**, 418 (2002)
173. K. Nomura, H. Ohta, A. Takagi, T. Kamiya, M. Hirano, H. Hosono, Nature **432**, 488 (2004)
174. H.Q. Chiang, J.F. Wager, R.L. Hoffman, J. Jeong, D.A. Keszler, Appl. Phys. Lett. **86**, 013503 (2005)
175. G. Thomas, Nature **389**, 907 (1997)
176. I. Satoh, T. Kobayashi, K. Katayma, T. Okada, T. Itoh, Appl. Phys. A **79**, 1445 (2004)